JOURNAL OF THE ROYAL SOCIETY Interface

rsif.royalsocietypublishing.org

Research

Cite this article: Zohdi TI. 2014 Mechanically driven accumulation of microscale material at coupled solid–fluid interfaces in biological channels. *J. R. Soc. Interface* **11**: 20130922. http://dx.doi.org/10.1098/rsif.2013.0922

Received: 8 October 2013
Accepted: 7 November 2013

Subject Areas:
bioengineering

Keywords:
accumulation, solid–fluid interfaces, channel flow

Author for correspondence:
T. I. Zohdi
e-mail: zohdi@me.berkeley.edu

Royal Society Publishing

Mechanically driven accumulation of microscale material at coupled solid–fluid interfaces in biological channels

T. I. Zohdi

Department of Mechanical Engineering, University of California, 6195 Etcheverry Hall, Berkeley, CA 94720-1740, USA

The accumulation of microscale materials at solid–fluid interfaces in biological channels is often the initial stage of certain growth processes, which are present in some forms of atherosclerosis. The objective of this work is to develop a relatively simple model for such accumulation, which researchers can use to qualitatively guide their analyses. Specifically, the approach is to construct rate equations for the accumulation at the solid–fluid interface as a function of the intensity of the shear stress. The accumulation of material subsequently reduces the cross-sectional area of the channel until the fluid-induced shear stress at the solid–fluid interface reaches a critical value, which terminates the accumulation rate. Characteristics of the model are explored analytically and numerically.

1. Introduction

The primary objective of this work is to model a 'generic' solid–fluid interface accumulation in biological channels, which contains flowing fluids with suspensions, and to develop a model that is relatively easy to evaulate. In some forms of growth, the first stage is attributed to accumulation of microscale suspensions in the fluid which adhere to the flow boundaries (walls). It is this stage, *accumulation*, that is the focus of this work. For example, one important application that motivates the present analysis is plaque growth because of high low-density lipoproteins (LDL) content. The phenomena of plaque build-up are thought to be due to a relatively high concentration of microscale suspensions (LDL particles) in blood. Plaques with high risk of rupture are termed *vulnerable*. Atherosclerotic plaque formation involves: (I) adhesion of monocytes (essentially larger suspensions) to the endothelial surface, which is controlled by the adhesion molecules stimulated by the excess LDL, as well as the oxygen content and the intensity of the blood flow, (II) penetration of the monocytes into the intima and subsequent tissue inflammation and (III) rupture of the plaque, accompanied by some level of thrombus formation and possible subsequent occlusive thrombosis. For surveys of plaque-related work, see the earlier studies [1–11]. The mechanisms involved in the early part of plaque formation (stage (I)) have not been extensively studied, although some qualitative studies have been carried out (e.g. [12,13]). Another related problem that motivates the upcoming analysis is calcification in the aortic valve. The deposition of calcium and fatty deposits on the valve, in relation to the shear stress on the leaflet wall, and how this leads to different tendencies of growth on the sides of the leaflet (facing the aorta or left ventricles) is an open question of increasing interest (e.g. [14–17]).

The approach in the present work is to develop rate equations for the accumulation of suspended microscale material at the solid–fluid interface. In the model, the intensity of the shear stress at the interface dictates the rate of accumulation. As a channel cross section narrows, the flow rate becomes more intense, thus naturally limiting the accumulation. Both analytical and numerical approaches are undertaken to determine the model's characteristics.

2. The basic model

Consider an idealized channel with a circular cross section of (initial) area $A_0 = \pi R_0^2$ with an initial solid–fluid radius R_0 (figure 1). The objective is to

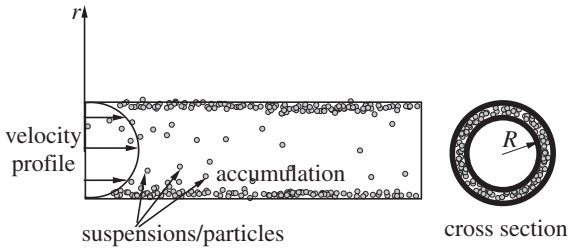

Figure 1. Flow through a channel with solid–fluid interface accumulation.

describe the mechanism by which A_0 changes, via a reduction in R_0, owing to wall accumulation caused by microscale deposits building up onto the channel's interior surface. The interior channel (solid–fluid interface) radius, denoted R, changes over time ($R(t=0)=R_0$). As a simplification, we assume that, at a given location along the channel, the accumulation is radially symmetric, and that at a given longitudinal (z) location, at the wall, $r=R$, and that we have a velocity profile given by a classical channel-flow of the form

$$v = v_{\max}\left(1-\left(\frac{r}{R}\right)^q\right), \tag{2.1}$$

where $v_{\max}$ is the centreline velocity. For fully developed laminar flow, $q=2$, while for increasing q one characterizes, phenomenologically, progressively turbulent flow ($q \geq 2$). The shear stress is given by

$$\tau = \mu\frac{\partial v}{\partial r} = -\frac{\mu v_{\max} q}{R}\left(\frac{r}{R}\right)^{q-1}. \tag{2.2}$$

The (reaction) stress at the wall (at $r=R$) is $\tau_{\rm w} = -\tau(r=R) = {}_{\max}q/R$. We will further assume that the overall flow rate is assumed constant

$$Q = \int_A v\,\mathrm{d}A = Q_0. \tag{2.3}$$

One can show that

$$v_{\max} = \frac{Q_0(q+2)}{Aq} = \frac{Q_0(q+2)}{\pi R^2 q}. \tag{2.4}$$

The stress at the wall becomes

$$\tau_{\rm w} = -\tau(r=R) = \frac{\mu v_{\max} q}{R} = \frac{\mu Q_0(q+2)}{\pi R^3}. \tag{2.5}$$

We have the following observations:

— increasing μ, Q_0 or q increases the stress at the wall ($\tau_{\rm w}$),
— increasing q leads to an increasingly more blunted flow profile and
— decreasing R increases the stress at the wall ($\tau_{\rm w}$).

Remark. In the next few sections, we will assume that the flow profile exponent (q) is independent of velocity. However, later in the presentation, we will relax this restriction and correlate q to the centreline Reynolds' number (Re).

3. Rate of interface accumulation

It is assumed that the tendency for material to adhere to the wall is controlled by the intensity of the shear stress near the wall. Essentially, higher shear stresses reduce the likelihood of material adhering to the wall, whereas lower shear stresses increase the tendency of material to adhere to the wall. Accordingly, we consider the accumulation rate to be proportional to the non-dimensionalized fractional difference between the shear stress at the wall (at a fixed z-location) and the critical 'detachment' stress ($\tau^* > 0$). Specifically, for the reduction of the solid–fluid radius

$$\begin{aligned}\frac{\mathrm{d}R}{\mathrm{d}t} &= -\eta\max\left(\frac{\tau^*-\tau_{\rm w}}{\tau^*},0\right)\\ &= -\eta\max\left(1-\frac{\mu Q_0(q+2)}{\pi\tau^* R^3},0\right),\end{aligned} \tag{3.1}$$

where $R_0 - R(t)$ is the reduction in radius (figure 1) and η is a rate constant representing the accumulation per unit time. As the velocity increases (increasing the shear stress), the microscale material in the fluid is less likely to adhere. We have the following observations:

— increasing τ^* increases the rate of adhesion,
— the unilateral limiter $\tau_w \geq \tau^*$ in equation (3.1) shuts off the accumulation at the solid–fluid interface,
— the rate of accumulation decreases with increasing μ, Q_0 and q and
— the rate of accumulation decreases with decreasing R.

Remark 3.1. Assuming that $\tau_w < \tau^*$, the accumulation equation has the following form:

$$\frac{\mathrm{d}R}{\mathrm{d}t} = -\eta\left(1-\frac{\mu Q_0(q+2)}{\pi\tau^* R^3}\right) = \frac{a_1}{R^3} - a_2 \stackrel{\rm def}{=} \mathcal{F}(R), \tag{3.2}$$

where $a_1 = (\eta\mu Q_0(q+2))/\pi\tau^*$ and $a_2 = \eta$. If we linearize $\mathcal{F}(R)$ about $R_0 = R(t=0)$, and we obtain

$$\frac{\mathrm{d}R^L}{\mathrm{d}t} \approx b_1 R^L + b_2, \tag{3.3}$$

where the superscript L indicates a linearized value and $b_1 = -(3a_1/R_0^4)$ and $b_2 = (4a_1/R_0^3) - a_2$. Using standard techniques (superposing homogeneous and particular solutions), we obtain

$$\begin{aligned}R^L(t) = &\left(-\frac{R_0}{3}+\frac{\pi R_0^4\tau^*}{3\eta\mu Q_0(q+2)}\right)\mathrm{e}^{-(3/R_0^4)((\mu Q_0(q+2)/\pi\tau^*))t}\\ &+\frac{4}{3}R_0 - \frac{\pi R_0^4\tau^*}{3\mu Q_0(q+2)}.\end{aligned} \tag{3.4}$$

Clearly, the rate of decay (of R) is dictated by η, and that decay is expected to be exponential. Beyond that, the linearized solution provides little insight into the character of general model, which is treated numerically next.

Remark 3.2. The steady-state value of the solid–fluid interface, denoted $R^{\rm ss}$, can be determined by setting $\mathrm{d}R/\mathrm{d}t = 0$, leaving

$$\begin{aligned}\frac{\mathrm{d}R}{\mathrm{d}t} = 0 \Rightarrow \tau^* = \tau_{\rm w} \Rightarrow \tau^* &= \frac{\mu Q_0(q+2)}{\pi(R^{\rm ss})^3}\\ \Rightarrow R^{\rm ss} &\stackrel{\rm def}{=} \left(\frac{\mu Q_0(q+2)}{\pi\tau^*}\right)^{1/3},\end{aligned} \tag{3.5}$$

which illustrates

— the steady-state value $R^{\rm ss}$ is independent of η,
— increasing the detachment stress threshold (τ^*) leads to more accumulation (reduction of $R^{\rm ss}$), with an inverse cubic dependency and
— increasing μ, Q_0 and q leads to less accumulation (larger $R^{\rm ss}$) with a cubic dependency.

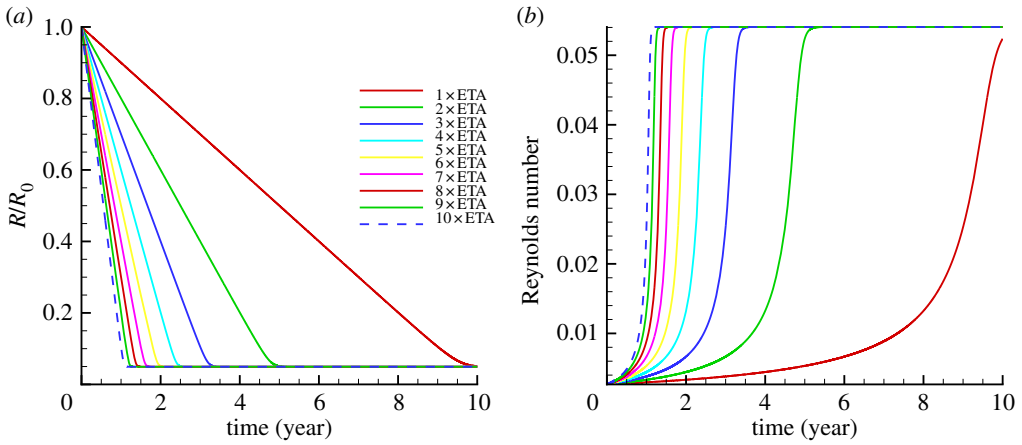

Figure 2. For $\eta = 10^{-3}/\phi$ m s^{-1} (*a*) the evolution of the radius for various accumulation rates and (*b*) the evolution of the centreline Reynold's number, $Re = (\rho v_{max} 2R/\mu) \times 10^{-6}$ for various accumulation rates. The dashed curve on the left corresponds to the highest value of η, while the curve on the right is for the lowest value of η. The curves in between progress monotonically from the highest to the lowest values of η. (Online version in colour.)

Remark 3.3. One can compute the amount of change of R^{ss} owing to changes in the parameters from the sensitivities to the parameters in the system

$$\text{viscosity: } \delta R^{ss}(\delta\mu) = \frac{\partial R^{ss}}{\partial \mu}\delta\mu, \quad \text{where}$$

$$\frac{\partial R^{ss}}{\partial \mu} = \frac{1}{3}\left(\frac{Q_0(q+2)}{\pi\tau^*}\right)^{1/3}\mu^{-2/3},$$

$$\text{flow-rate: } \delta R^{ss}(\delta Q_0) = \frac{\partial R^{ss}}{\partial Q_0}\delta Q_0,$$

$$\text{where } \frac{\partial R^{ss}}{\partial Q_0} = \frac{1}{3}\left(\frac{\mu(q+2)}{\pi\tau^*}\right)^{1/3} Q_0^{-2/3},$$

$$\text{flow profile exponent: } \delta R^{ss}(\delta q) = \frac{\partial R^{ss}}{\partial q}\delta q,$$

$$\text{where } \frac{\partial R^{ss}}{\partial Q_0} = \frac{1}{3}\left(\frac{\mu Q_0}{\pi\tau^*}\right)^{1/3}(q+2)^{-2/3}$$

and

$$\text{shear stress threshold: } \delta R^{ss}(\delta\tau^*) = \frac{\partial R^{ss}}{\partial \tau^*}\delta\tau^*,$$

$$\text{where } \frac{\partial R^{ss}}{\partial Q_0} = -\frac{1}{3}\left(\frac{\mu Q_0(q+2)}{\pi}\right)^{1/3}(\tau^*)^{-4/3}.$$

Furthermore, the ratios of the sensitivities provide information on the relative sensitivity of one parameter to another, for example

$$\text{flow-rate/viscosity: } \frac{\delta R^{ss}(\delta Q_0)}{\delta R^{ss}(\delta\mu)} = \frac{\mu}{Q_0}\frac{\delta Q_0}{\delta\mu},$$

$$\text{flow profile exponent/viscosity: } \frac{\delta R^{ss}(\delta q)}{\delta R^{ss}(\delta\mu)} = \frac{\mu}{(q+2)}\frac{\delta q}{\delta\mu}$$

and

$$\text{shear stress threshold/viscosity: } \frac{\delta R^{ss}(\delta\tau^*)}{\delta R^{ss}(\delta\mu)} = \frac{\mu}{\tau^*}\frac{\delta\tau^*}{\delta\mu}.$$

This allows one to determine the amount of change of one parameter, say δQ_0 that would be needed to make a comparable change δR^{ss} due to say $\delta\mu$ by computing

$$\frac{\delta R^{ss}(\delta Q_0)}{\delta R^{ss}(\delta\mu)} = \frac{\mu}{Q_0}\frac{\delta Q_0}{\delta\mu} = 1 \Rightarrow \delta Q_0 = \delta\mu\frac{Q_0}{\mu}. \tag{3.6}$$

The procedure is virtually identical for the other parameters in the system.

4. Direct time-transient numerical simulation

The general form of the equation

$$\frac{dR}{dt} = \mathcal{F}(R) = -\eta\max\left(1 - \frac{\mu Q_0(q+2)}{\pi\tau^* R^3}, 0\right) \tag{4.1}$$

is solved using an explicit forward Euler time integration of the form

$$R(t+\Delta t) = R(t) + \Delta t\mathcal{F}(R(t)). \tag{4.2}$$

The simulation time was set to 10 years.[1] An extremely small (relative to the total simulation time) time-step size of $5 \times 10^{-4}\,\phi$, where $\phi = 3600 \times 24 \times 365$ is the number of seconds in a year, was used. Further reductions of the time-step size produced no notable changes in the results, thus the solutions generated can be considered to have negligible numerical error. The following physical parameters were used:

— $R(t=0) = R_0 = 0.01$ m,
— $Q_0 = \int_{A_0} v\,dA = \pi R_0^2 v_m(t=0)$ m^3 s^{-1}, where $v_m(t=0) = 0.1$ m s^{-1} in the mean velocity,
— $\mu = 0.003$ Pa s^{-1},
— $\tau^* = 1$ kPa,
— $\rho = 10^3$ kg m^{-3} and
— $\eta = \dfrac{10^{-3}}{\phi}$ m s^{-1}.

The results are shown in figure 2. As indicated in figure 2, eventually, the accumulation slows, then terminates, once the channel narrows sufficiently to raise the fluid-induced shear stress to exceed the threshold value of τ^*. For the set of parameters chosen, the initial centreline velocity is $v_{max} = 0.2$ m s^{-1} and ramps up to $v_{max} = 82.207$ m s^{-1} owing to the reduction of the cross section and the constant volumetric flow rate $Q = Q_0$ (figure 3). Realistically, as the cross-sectional narrows, the flow becomes relatively more turbulent, i.e. the Reynolds' number increases. The exponent q must then also change from a quadratic profile a more blunted profile. To incorporate this effect, we introduce a dependency of q on the centreline Reynolds number shortly. This will have the effect of further accumulation rate limitation. Clearly, for increasing η, the rate of accumulation increases, and the time to steady-state decreases. While figure 2 illustrates the basic behaviour with respect to variations in the accumulation rate parameter, there are clearly other possible parameters to vary, and we refer the reader to §3 pertaining to a sensitivity analysis.

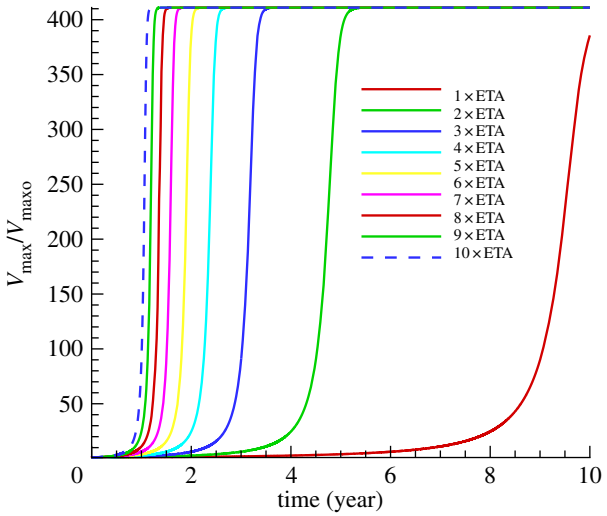

Figure 3. For $\eta = 10^{-3}/\phi$ m s^{-1}: the evolution of v_{max} for various accumulation rates. The dashed curve on the left corresponds to the highest value of η, while the curve on the right is for the lowest value of η. The curves in between progress monotonically from the highest to the lowest values of η. (Online version in colour.)

Remark. We note that one can write the time needed to reach a given value of $R(t^*) = R^*$ in terms of the following integral:

$$t = \int_{R(t=0)}^{R^*} \frac{\pi R^3 \tau^*}{\eta(\mu Q_0(q+2) - \tau^* \pi R^3)} \mathrm{d}R, \tag{4.3}$$

which can be numerically integrated, however, this timescale can also be inferred easily from figure 2.

5. Model extensions: rate limiting effects—blunted velocity profile evolution

Clearly as the Reynolds number increases, the velocity profile will change from a quadratic ($q = 2$) to a more blunted profile ($q \gg 2$), which represents, phenomenologically, turbulent (inertia-dominated) behaviour (figure 4).

5.1. Incorporating profile changes

The effect of a changing profile is described by representing q by a linear function of the centreline Reynolds' number (Re)

$$q = q(Re) = c_1 Re + c_2, \tag{5.1}$$

where $Re = \rho v_{max} 2R/\mu$ and c_1 and c_2 are constants. Models of this type, linking the the profile exponent (q) to the centreline Reynolds' number (Re), are quite well-established (e.g. [18]). Usually, $0 \leq c_1 \ll 1$ and $c_2 \approx 2$, and in the limit we have, for $c_1 = 0$ and $c_2 = 2$, laminar flow ($q = 2$). For the general case, combining equation (2.4) with equation (5.1) and the definition of the centreline Reynolds' number, we obtain a quadratic relationship for q,

$$q^2 - (\gamma + c_2)q - 2\gamma = 0, \tag{5.2}$$

where $\gamma = 2c_1 Q_0 \rho/\pi R\mu$. This quadratic relationship can be solved in closed form for q to yield[2]

$$q(Re) = \tfrac{1}{2}\left((\gamma + c_2) \pm \sqrt{(\gamma + c_2)^2 + 8\gamma}\right). \tag{5.3}$$

Clearly, the larger root is the physically correct choice. $Q(Re)$ is clearly a function of R^{-1} and decreasing R increases q.

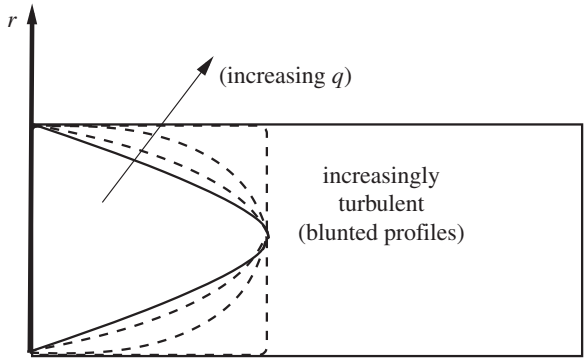

Figure 4. As the Reynolds number increases, the velocity profile will increase ($q > 2$).

5.2. Numerical examples

The general form of the equation

$$\frac{\mathrm{d}R}{\mathrm{d}t} = \mathcal{F}(R) = -\eta \max\left(1 - \frac{\mu Q_0((\frac{1}{2}(\gamma(R) + c_2) + \sqrt{(\gamma(R) + c_2)^2 + 8\gamma(R)}) + 2)}{\pi \tau^* R^3}, 0\right) \tag{5.4}$$

is solved using a forward Euler time integration, $R(t + \Delta t) = R(t) + \Delta t \mathcal{F}(R(t))$. The same parameters as for the $q \neq q(Re)$ case were used, with the two additional parameters for the change of flow profile with Reynolds' number, $c_1 = 10^{-2}$ and $c_2 = 2$. Figures 5 and 6 illustrate the rate limiting effect of the blunting of the flow profile (increasingly more turbulent flow), relative to the case where q is not a function of the flow velocity (figures 2 and 3). For the set of parameters chosen, the initial centreline velocity is $v_{max} = 0.2$ m s^{-1} and ramps up to $v_{max} = 9.716$ m s^{-1}, which is much more realistic than the constant q model which predicts $v_{max} = 82.207$ m s^{-1}. Numerically, the solution of this more relatively complex model $q = q(Re)$ requires virtually no additional effort relative to $q \neq q(Re)$. One could attempt to analytically extract the steady-state value of R by setting $\mathrm{d}R/\mathrm{d}t = 0$ and combining it with equation (5.3), leaving

$$R^3 = \frac{\mu Q_0(q(Re) + 2)}{\pi \tau^*} = \frac{\mu Q_0(\frac{1}{2}((\gamma(R) + c_2) + \sqrt{(\gamma(R) + c_2)^2 + 8\gamma(R)}) + 2)}{\pi \tau^*}. \tag{5.5}$$

However, this leads to a highly nonlinear equation, with multiple roots, that would have to be solved numerically. Clearly, it is easier to simply track the steady-state value of R from figure 5.

6. Conclusion

As indicated at the beginning of this paper, the primary objective of this communication was to investigate solid–fluid interface accumulation on the walls of biological channels and to develop a model that researchers in the field can easily implement and use to guide experiments. Semi-analytical relationships were also developed which characterize accumulation and flow-induced rate limitations,

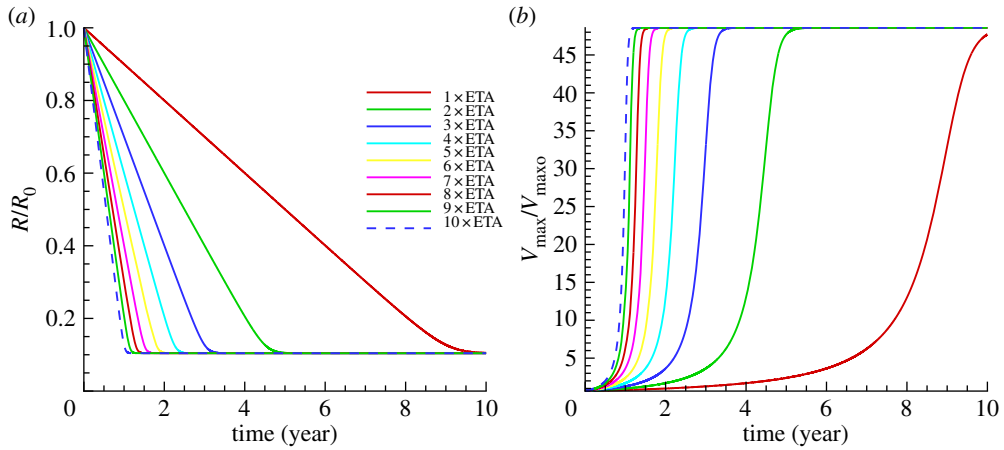

Figure 5. For $q = q(Re)$ and $\eta = 10^{-3}/\phi$ m s^{-1}: (*a*) the evolution of the radius for various accumulation rates and (*b*) the evolution of v_{max} for various accumulation rates. The dashed curve on the left corresponds to the highest value of η, while the curve on the right is for the lowest value of η. The curves in between progress monotonically from the highest to the lowest values of η. (Online version in colour.)

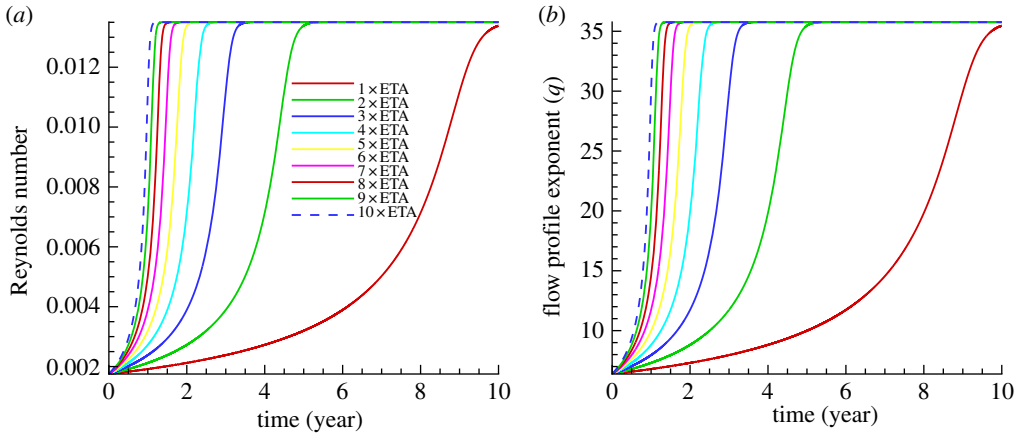

Figure 6. For $q = q(Re)$ and $\eta = 10^{-3}/\phi$ m s^{-1}: (*a*) the evolution of the centreline $Re = \rho v_{max} 2R/\mu \times 10^{-6}$ for various accumulation rates and (*b*) the evolution of flow exponent for various accumulation rates. The dashed curve on the left corresponds to the highest value of η, while the curve on the right is for the lowest value of η. The curves in between progress monotonically from the highest to the lowest values of η. (Online version in colour.)

owing to the more intense flows for smaller (occluded) cross sections. This is useful because of the long-term character of experiments involved with tracking accumulation. Future work should concentrate on the development of a subsequent growth model, involving both adhesion as well as constitutive growth (e.g. [19–23]). It is also important to explore how growth depends on temporal/spatial gradients of wall shear stress. These processes probably involve strongly coupled diffusive, chemical effects and thermal effects, and we refer the reader to Markenscoff [24–26] for in depth mathematical analysis of such coupled systems. There are conflicting reports on whether high or low shear stress correlates with growth. Certainly, there may be scenarios where growth is controlled by low shear stress in one phase and high shear stress in another. Clearly, the mechanism for biological attachment is quite involved, and the simple notion used in this paper of a critical attachment/detachment stress threshold may be inadequate. Therefore, models building upon results such as those found in Hermanowicz [27–29], Sawyer & Hermanowicz [30] and Yoon & Mofrad [31] may prove quite useful in this regard.

The presented analysis and model can provide a useful guide to designing and interpreting experiments, which can take years. However, while the model can provide qualitative *a priori* information for further computationally intensive large-scale simulations, extensions are invariably going to require complex spatial discretization of the system under analysis and could also entail resolving particle–fluid interaction. The number of research areas involving particles in a fluid undergoing various coupled processes is immense, and it would be futile to attempt to catalogue all of the various applications. However, a common characteristic of such systems is that the various physical fields (thermal, mechanical, chemical, etc.) are strongly coupled, with particles that tend to agglomerate (cluster). In Zohdi [32], a flexible and robust solution strategy was developed to resolve coupled systems comprising large groups of flowing particles embedded within a fluid, based on agglomeration models found in Zohdi [33]. In that analysis, particles were surrounded by a continuous interstitial fluid which is assumed to obey the compressible Navier–Stokes equations. Thermal effects were also considered. Such particle/fluid systems are strongly coupled because of the mechanical forces induced by the fluid onto the particles and vice-versa. Because the coupling of the various particle and fluid fields can dramatically change over the course of a flow process, a primary focus of that work was the development of a recursive 'staggering' solution scheme, whereby the time-steps were adaptively adjusted to control the error associated with the incomplete resolution of the coupled interaction between the various solid particulate and continuum fluid fields. The approach is straightforward and can be easily

incorporated within any standard computational fluid mechanics code based on finite difference, finite-element, finite volume or discrete-element discretization, for example, those developed in earlier studies [34–39].

Endnotes

[1]These long timescales are motivated by atherosclerosis applications.
[2]Note that for laminar flow ($c_1 = 0$ and $c_2 = 2$) there are two roots to equation (5.3), $q = 2$ and $q = 0$.

References

1. Chyu KY, Shah PK. 2001 The role of inflammation in plaque disruption and thrombosis. *Rev. Cardiovas. Med.* **2**, 82–91.
2. Davies MJ, Richardson PD, Woolf N, Katz DR, Mann J. 1993 Risk of thrombosis in human atherosclerotic plaques: role of extracellular lipid, macrophage, and smooth muscle cell content. *Br. Heart Journal.* **69**, 377–381. (doi:10.1136/hrt.69.5.377)
3. Fuster V. 2002 *Assessing and modifying the vulnerable atherosclerotic plaque*. Armonk, NY: Futura publishing company.
4. Libby P. 2001 Current concepts of the pathogenesis of the acute coronary syndromes. *Circ.* **104**, 365–372. (doi:10.1161/01.CIR.104.3.365)
5. Libby P. 2001 The vascular biology of atherosclerosis. In *Heart disease: a textbook of cardiovascular medicine* (eds E Braunwald, DP Zipes, P Libby), 6th edn, ch. 30, pp. 995–1009. Philadelphia, PA: W. B. Saunders Company.
6. Libby P, Ridker PM, Maseri A. 2002 Inflammation and atherosclerosis. *Circulation* **105**, 1135–1143. (doi:10.1161/hc0902.104353)
7. Libby P, Aikawa M. 2002 Stabilization of atherosclerotic plaques: new mechanisms and clinical targets. *Nat. Med.* **8**, 1257–1262. (doi:10.1038/nm1102-1257)
8. Loree HM, Kamm RD, Stringfellow RG, Lee RT. 1992 Effects of fibrous cap thickness on peak circumferential stress in model atherosclerotic vessels. *Circ. Res.* **71**, 850–858. (doi:10.1161/01.RES.71.4.850)
9. Richardson PD, Davies MJ, Born GVR. 1989 Influence of plaque configuration and stress distribution on fissuring of coronary atherosclerotic plaques. *Lancet* **2**, 941–944. (doi:10.1016/S0140-6736(89)90953-7)
10. Shah PK. 1997 Plaque disruption and coronary thrombosis: new insight into pathogenesis and prevention. *Clin. Cardiol.* **20**(Suppl. II), 38–44.
11. van der Wal AC, Becker AE. 1999 Atherosclerotic plaque rupture—pathologic basis of plaque stability and instability. *Cardiovasc. Res.* **41**, 334–344. (doi:10.1016/S0008-6363(98)00276-4)
12. Zohdi TI, Holzapfel GA, Berger SA. 2004 A phenomenological model for atherosclerotic plaque growth and rupture. *J. Theor. Biol.* **227**, 437–443. (doi:10.1016/j.jtbi.2003.11.025)
13. Zohdi TI. 2005 A simple model for shear stress mediated lumen reduction in blood vessels. *Biomech. Model. Mechanobiol.* **4**, 57–61. (doi:10.1007/s10237-004-0059-2)
14. Weinberg EJ, Schoen FJ, Mofrad MRK. 2009 A computational model of aging and calcification in the aortic heart valve. *PLoS ONE* **4**, e5960. (doi:10.1371/journal.pone.0005960)
15. Wenk JF, Papadopoulos P, Zohdi TI. 2010 Numerical modeling of stress in stenotic arteries with microcalcifications: a micromechanical approximation. *J. Biomech. Eng.* **133**, 014503.
16. Klepach D, Lee LC, Wenk J, Ratcliffe M, Zohdi TI, Navia J, Kassab G, Kuhl E, Guccione JM. 2012 Growth and remodeling of the left ventricle: a case study of myocardial infarction and surgical ventricular restoration. *Mech. Res. Commun.* **42**, 134–141. (doi:10.1016/j.mechrescom.2012.03.005)
17. Lee LC *et al*. 2013 Analysis of patient-specific surgical ventricular restoration—importance of an ellipsoid left ventricular geometry for diastolic and systolic function. *J. Appl. Physiol.* **115**, 136–144. (doi:10.1152/japplphysiol.00662.2012)
18. Hinze JO. 1975 *Turbulence*. New York, NY: McGraw-Hill.
19. Ambrosi D *et al*. 2011 Perspectives on biological growth and remodeling. *J. Mech. Phys. Solids* **59**, 863–883. (doi:10.1016/j.jmps.2010.12.011)
20. Göktepe S, Abilez OJ, Parker KK, Kuhl E. 2010 A multiscale model for eccentric and concentric cardiac growth through sarcomerogenesis. *J. Theor. Biol.* **265**, 433–442. (doi:10.1016/j.jtbi.2010.04.023)
21. Menzel A, Kuhl E. 2012 Frontiers in growth and remodeling. *Mech. Res. Commun.* **42**, 1–14. (doi:10.1016/j.mechrescom.2012.02.007)
22. Kuhl E, Maas R, Himpel G, Menzel A. 2007 Computational modeling of arterial wall growth: attempts towards patient specific simulations based on computer tomography. *Biomech. Model Mechanobiol.* **6**, 321–331. (doi:10.1007/s10237-006-0062-x)
23. Zöllner AM, Buganza Tepole A, Kuhl E. 2012 On the biomechanics and mechanobiology of growing skin. *J. Theor. Biol.* **297**, 166–175. (doi:10.1016/j.jtbi.2011.12.022)
24. Markenscoff X. 2001 Diffusion induced instability. *Q. Appl. Mech.* **LIX**, 147–151.
25. Markenscoff X. 2001 Instabilities of a thermo-mechano-chemical system. *Q. Appl. Mech.* **LIX**, 471–477.
26. Markenscoff X. 2003 On conditions of 'negative creep' in amorphous solids. *Mech. Mater.* **35**, 553–557. (doi:10.1016/S0167-6636(02)00272-7)
27. Hermanowicz SW. 1999 Two-dimensional simulations of biofilm development: effects of external environmental conditions. *Water Sci. Technol.* **39**, 107–114. (doi:10.1016/S0273-1223(99)00157-2)
28. Hermanowicz SW. 2001 A simple 2D biofilm model yields a variety of morphological features. *Math. Biosci.* **169**, 1–14. (doi:10.1016/S0025-5564(00)00049-3)
29. Hermanowicz SW. 2004 Membrane filtration of biological solids: a unified framework and its applications to membrane bioreactors. In *Proc., Water Environment Membrane Technology 2004 Conf., 9 June 2004, Seoul, South Korea*.
30. Sawyer LK, Hermanowicz SW. 2000 Detachment of *Aeromonas hydrophila* and *Pseudomonas aeruginosa* due to variations in nutrient supply. *Water Sci. Technol.* **41**, 139–145.
31. Yoon SH, Chang J, Lin L, Mofrad MRK. 2011 A biological breadboard platform for cell adhesion and detachment studies. *Lab Chip* **11**, 3555. (doi:10.1039/c1lc20369j)
32. Zohdi TI. 2007 Computation of strongly coupled multifield interaction in particle–fluid systems. *Comp. Methods Appl. Mech. Eng.* **196**, 3927–3950. (doi:10.1016/j.cma.2006.10.040)
33. Zohdi TI. 2004 A computational framework for agglomeration in thermo-chemically reacting granular flows. *Proc. R. Soc. A* **460**, 3421–3445. (doi:10.1098/rspa.2004.1277)
34. Kaazempur-Mofrad MR, Wada S, Myers JG, Ethier CR. 2005 Blood flow and mass transfer in arteries with axisymmetric and asymmetric stenoses. *International J. Heat Mass Transfer* **48**, 4510–4517. (doi:10.1016/j.ijheatmasstransfer.2005.05.004)
35. Kaazempur-Mofrad MR, Younis HF, Isasi AG, Chan RC, Hinton DP, Sukhova G, LaMuraglia GM, Lee RT, Kamm RD. 2004 Characterization of the atherosclerotic carotid bifurcation using MRI, finite element modeling and histology. *Ann. Biomed. Eng.* **32**, 932–946. (doi:10.1023/B:ABME.0000032456.16097.e0)
36. Kaazempur-Mofrad MR, Younis HF, Patel S, Isasi AG, Chung C, Chan RC, Hinton DP, Lee RT, Kamm RD. 2003 Cyclic strain in human carotid bifurcation and its potential correlation to atherogenesis: idealized and anatomically-realistic models. *J. Eng. Math.* **47**, 299–314. (doi:10.1023/B:ENGI.0000007974.82115.16)
37. Onate E, Idelsohn SR, Celigueta MA, Rossi R. 2008 Advances in the particle finite element method for the analysis of fluid–multibody interaction and bed erosion in free surface flows. *Comp. Methods Appl. Mech. Eng.* **197**, 1777–1800. (doi:10.1016/j.cma.2007.06.005)
38. Onate E, Celigueta MA, Idelsohn SR, Salazar F, Surez B. 2011 Possibilities of the particle finite element method for fluid–soil–structure interaction problems. *Comput. Mech* **48**, 307–318. (doi:10.1007/s00466-011-0617-2)
39. Avci B, Wriggers P. 2011 A DEM-FEM coupling approach for the direct numerical simulation of 3D particulate flows. *J. Appl. Mech.* **79**, 010901. (doi:10.1115/1.4005093)